J Mater Sci (2017) 52:6670–6686

Effects of extrusion ratio and annealing treatment on the mechanical properties and microstructure of a Mg–11Gd–4.5Y–1Nd–1.5Zn–0.5Zr (wt%) alloy

Zijian Yu[1], Yuanding Huang[2], Weimin Gan[2], Zhengye Zhong[3], Norbert Hort[2], and Jian Meng[1,*]

[1] *State Key Laboratory of Rare Earth Resources Utilization, Changchun Institute of Applied Chemistry, Chinese Academy of Sciences, Changchun 130022, People's Republic of China*

[2] *Institute of Materials Research, Helmholtz-Zentrum Geesthacht, Max-Planck-Str. 1, 21502 Geesthacht, Germany*

[3] *Institute for Materials Science and Engineering, Clausthal University of Technology, 38678 Clausthal-Zellerfeld, Germany*

Received: 11 November 2016
Accepted: 7 February 2017
Published online: 16 February 2017

ABSTRACT

This study investigates the effects of the extrusion ratio and annealing treatment on the microstructure, texture and mechanical properties of an as-extruded Mg–11Gd–4.5Y–1Nd–1.5Zn–0.5Zr (wt%) alloy. A high extrusion ratio (30:1) results in a homogeneous microstructure with fine dynamic recrystallized (DRXed) grains, while a low extrusion ratio (6:1) leads to a bimodal microstructure with un-DRXed regions and DRXed grains. The bimodal microstructure can be removed by subsequent annealing. This alloy contains several long-period stacking ordered (LPSO) and Mg_5RE phases (RE: rare earth). The extrusion ratio and annealing process have negligible effects on the volume fraction of the LPSO phase but have significant effects on the Mg_5RE phase. The volume fraction of the Mg_5RE phase decreases as the extrusion ratio and annealing time increase. Cuboid precipitates form in the alloy extruded at low extrusion ratios after annealing. The alloy exhibits a bimodal texture with <0001> and $<10\bar{1}0>$ components. The presence of the <0001> component is determined by a critical grain size. The texture evolution (such as the degree of grain growth) is not influenced by the extrusion ratio, but it is affected by the annealing time, which is related to the Mg_5RE phase rather than the LPSO phase. The grain refinement, the Mg_5RE and LPSO phases, and the texture contribute to the alloy strengthening. Finally, a high-strength extruded Mg bar with a diameter of 32 mm (an extrusion ratio of 6:1) was successfully produced.

Address correspondence to E-mail: jmeng@ciac.ac.cn

DOI 10.1007/s10853-017-0902-3

Introduction

Mg alloys have attracted considerable attention due to their great potential in structural applications. The competitive features of Mg alloys, such as low density, high specific strength and excellent castability, have led to their increased utilization in the automobile and aerospace industries [1]. Hot extrusion, as an efficient, economic and advanced processing method for wrought Mg alloys, has been studied for decades. This process not only adjusts the grains and particles but also modifies the texture of the alloy [2, 3]. In addition, hot extrusion can significantly improve the mechanical properties of Mg alloys due to the fact that fine dynamic recrystallized (DRXed) grains and homogeneously dispersed particles are achieved after extrusion [4–6]. The extrusion conditions, such as the extrusion ratio and temperature, largely determine the performance of the as-extruded alloys [7–10]. Chen et al. [7] revealed that the mechanical properties of the AZ31 alloy are significantly improved by increasing the extrusion ratio. Shahzad et al. [8] reported that the ductility of the AZ80 alloy can be enhanced when the texture is weakened by increasing the extrusion ratio. Robson et al. [2] observed that the extrudates produced with a high extrusion ratio and a low extrusion temperature show an unusual texture in which the *c*-axis is parallel to the extrusion direction (ED). This texture was suggested as a recrystallization texture that has a growth advantage over other texture components. This texture provides poor crystallographic alignment for basal slip under both tension and compression, leading to low room-temperature ductility. Alizadeh et al. [3] explained that the formation of this unusual texture is related to the solute drag effect and the grain boundary pinning effect of the second phase precipitates. This unusual texture was also reported in our previous work [6]. However, the reason for its formation remains unclear and requires further investigation.

Mg–rare earth (RE) alloys, such as Mg–Gd–Y, Mg–Y–Nd and Mg–Gd–Nd systems, exhibit an attractive performance at room and elevated temperatures [11–17]. Gd and/or Y additions exhibit remarkable strengthening effects because their high solubility in Mg (23.5 wt% for Gd and 12.5 wt% for Y at their eutectic temperatures) provides a strong age-hardening response and effective solution strengthening [12, 18]. In comparison with Gd or Y, Nd has a lower solubility of 3.6 wt% at the eutectic temperature [18]. Nd additions further improve the age-hardening response and strength of Mg–RE alloys by increasing the strengthening phase β' and β precipitates [19, 20]. The addition of Zn in Mg–RE alloys leads to the formation of the LPSO phase. This LPSO phase significantly increases the mechanical properties via short-fibre strengthening [21–23]. Moreover, the presence of the LPSO phase contributes to improvements in the heat resistance [24]. Recently, Homma et al. [4] successfully fabricated a high-strength Mg–10Gd–5.7Y–1.6Zn–0.5Zr (wt%) alloy by hot extrusion and ageing. This alloy exhibits a high yield stress (YS) of 473 MPa and an elongation to failure of 8.0% at room temperature. This high strength is primarily attributed to the grain refinement, fine metastable phase and LPSO phase. Yamasaki et al. [5] developed an as-extruded Mg–14Gd–2.33Zn (wt%) alloy with a high dispersion of the LPSO phase exhibiting a high YS of 345 MPa and an elongation to failure of 6.9%. Yu et al. [24] developed an as-extruded Mg–11Gd–4.5Y–1Nd–1.5Zn–0.5Zr (wt%) alloy having a YS of 316 MPa and an elongation to failure of 6.3% at 250 °C. The excellent mechanical properties at elevated temperatures are attributed to the presence of the LPSO and Mg_5RE phases. In addition, this alloy exhibits a YS of 502 MPa and an elongation to failure of 2.6% at room temperature [25]. Mg–Gd–Y-based alloys with Nd and Zn additions could be a promising candidate for producing high-strength and heat-resistant Mg alloys.

Texture plays an important role in influencing the mechanical behaviours of wrought Mg alloys. For conventional Mg alloys, such as AZ31 and AZ61, hot extrusion develops a sharp basal texture along the *c*-axis, perpendicular to the ED [26–28]. These textural grains provide a poor crystal orientation for basal slip and twinning in the tensile deformation along the ED, leading to high strength but low ductility. It is well known that the Mg alloys with RE additions exhibit excellent ductility, which is explained by two reasons [29–31]. First, the texture intensity is decreased, and second, the $<11\bar{2}1>$ RE texture is developed in which the $<11\bar{2}1>$ oriented grains are beneficial for basal slip. Although it has been shown that RE elements are the most effective texture modifiers, it is noteworthy that the most studied Mg–RE alloys are those with almost no second phases. The effects of texture on the mechanical properties of

Mg–RE alloys with several second phase particles are still unclear.

Annealing is another efficient method to modify the mechanical behaviours of wrought Mg alloys [32]. An annealing treatment is typically performed to optimize the deformed microstructure and to achieve the best combination of strength and ductility. The evolution of microstructures and textures related to the grain growth behaviour has been investigated extensively. Prado et al. [26, 27] suggested that the annealing treatment results in a strong basal texture and abnormal growth of the $\{11\bar{2}0\}$ grains. Wu et al. [33] observed that the abnormal growth of the $<11\bar{2}1>$ grains occurs during annealing and leads to the strengthening of the $<11\bar{2}1>$ RE texture. However, for Mg–RE alloys with several particles, the texture and microstructure evolutions during annealing are still not well understood. The effects of the annealing treatment on the mechanical properties must be further investigated.

In the present work, we investigated the high-strength and heat-resistant Mg–11Gd–4.5Y–1Nd–1.5Zn–0.5Zr (wt%) alloy, with the aim of gaining an in-depth understanding of the effects of the extrusion ratio and annealing treatment on the microstructure, second phase, texture and mechanical properties of the alloy. The influences of the second phase particles on the microstructural variations and texture evolutions during the extrusion and annealing processes were explored. The formation mechanism of the unusual texture, with the *c*-axis aligned parallel to the ED, was also discussed.

Experimental procedures

A Mg–11Gd–4.5Y–1Nd–1.5Zn–0.5Zr alloy was melted in an electrical furnace at 760 °C under a CO_2/SF_6 (99:1) atmosphere. After the melt was cooled to 720 °C, it was cast into a water-cooled mould with a diameter of 92 mm. The mould was preheated to 200 °C by a cylindrical heater (Φ 92 mm × 600 mm) before casting. The cylindrical billet was machined into round bars with diameters of 82 mm and lengths of 120 mm. The round bars were then homogenized at 535 °C for 24 h followed by quenching in water at 25 °C. The homogenized bars were preheated at 410 °C for 1 h before hot extrusion, which was performed at 410 °C with extrusion ratios of 6:1 and 30:1 at a ram speed of 1 mm s^{-1}. After hot extrusion was complete, annealing treatments were conducted at 450 °C for 24 and 72 h. Tensile specimens with gauge dimensions of 20 mm × 4 mm × 2 mm were tested at room temperature along the ED with a speed of 1 mm min^{-1} using an Instron 5569 testing machine. The microstructural observations were conducted by optical microscopy (OM) using a Leica DMI 5000 light optical microscope, scanning electron microscopy (SEM) using a Zeiss Ultra 55 SEM equipped with EDAX/TSL electron back scattered diffraction (EBSD) operating at 15 kV, and transmission electron microscopy (TEM) using FEI-TECNAI G^2 TEM operating at 200 kV. The metallographic samples were selected from the longitudinal section of the extruded bars. The TEM foils were prepared by mechanical grinding to a thickness of approximately 120 μm and then electropolished to perforation (2.5 vol% perchloric acid and 97.5 vol% ethanol, at −47 °C, 40 V) using a Fishionie twin-jet electropolisher. X-ray diffraction (XRD) measurements were obtained for the phase analysis using a diffractometer (Siemens D5000, 40 kV and 40 mA) with Cu Kα radiation and a secondary monochromator (step rate of 0.03 s^{-1}, dwell time of 3 s). The macro-texture measurements were conducted using high-energy X-ray (87 keV) with a wavelength of 0.0142 nm and an incident beam size of 200 × 200 μm^2 at the High Energy Material Science (HEMS) beamline of the Helmholtz-Zentrum Geesthacht experimental station P07B at PETRA III storage ring, at DESY (Deutsche Elektronen Synchrotron) in Germany [34]. The SEM-EBSD measurements (15 keV, step size 0.2 μm) were used to analyse the local microstructure and texture. To ensure statistical rigour, more than 1000 grains were examined for each condition. The specimens for the SEM-EBSD measurement were ground using silicon carbide emery paper up to a 2500 grit and then polished with 3-micron diamond and finally with a 0.05-micron silica solution (Struers OP-S suspension). In this study, the as-extruded samples are designated as E6 and E30, representing their extrusion ratios of 6:1 and 30:1, respectively. The annealed samples are designated as E6A1 and E30A1 after annealing for 24 h and as E6A2 and E30A2 after annealing for 72 h, respectively. The volume fraction of each second phase was calculated from the average area using SEM micrographs. The average grain size of the DRXed grains was calculated using the linear intercept method.

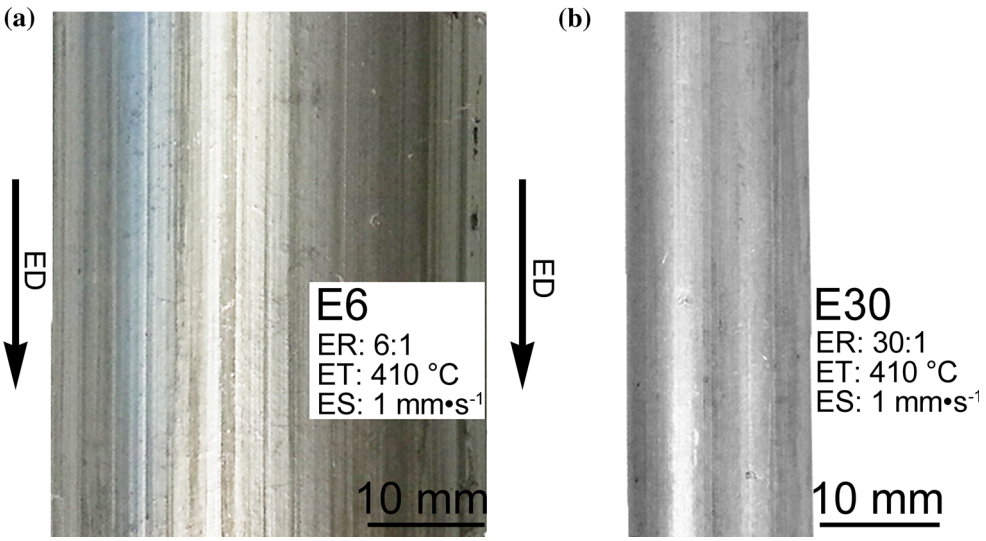

Figure 1 Extruded bars of samples: **a** E6 and **b** E30. *Note* that *ER* represents extrusion ratio, *ET* represents extrusion temperature, and *ES* represents extrusion speed.

Results

Microstructural characterizations

Microstructure after hot extrusion

Figure 1a, b shows the surface profiles of the studied alloy extruded with different extrusion ratios. Both extrudates exhibited smooth surfaces without any micro-cracks. To examine the effects of the extrusion ratio on the microstructure, the E6 and E30 samples were observed using OM and SEM (Fig. 2a–f). The OM and SEM micrographs show that several fine particles and some rod-like particles formed in both of the E6 and E30 samples. The rod-like particles with a large aspect ratio were aligned parallel to the ED, and the fine particles were distributed at the grain boundaries. The recrystallization was not completed at the low extrusion ratio of 6:1 (Fig. 2a, c, e), as the E6 sample exhibited a bimodal microstructure consisting of DRXed grains and un-DRXed regions. Several plate-like particles were densely dispersed in the un-DRXed regions, as shown in Fig. 2e. Compared with sample E6, sample E30 exhibited a recrystallized microstructure fully consisting of the fine DRXed grains (Fig. 2b, d, f).

To analyse the segregation of the solute atoms and chemical compositions of the second phases, energy-dispersive X-ray spectroscopy (EDS) elemental mapping was conducted in the square area I shown in Fig. 2c. In the EDS maps, the typical rod-like particles, plate-like particles and fine particles are highlighted by rectangles, ellipses and arrows, respectively (Fig. 3). Both the plate-like particles and the fine particles were composed of the elements Mg, Gd, Y and Nd, while the rod-like particles contained these elements in addition to Zn. Identification of the phases was further conducted by XRD, revealing that the identical phase constitution included Mg, Mg_5RE and $Mg_{12}REZn$ phases in the E6 and E30 samples (Fig. 4). According to the different enrichments of Zn in each phase, the rod-like particles can be indexed as the $Mg_{12}REZn$ phase, while the fine particles and plate-like particles should be the Mg_5RE phase. The TEM micrographs show a typical rod-like particle at the grain boundaries and the corresponding selected area electron diffraction (SAED) pattern along the $<11\bar{2}0>_{\alpha\text{-Mg}}$ (Fig. 5a). The rod-like particles exhibit a 14H-type LPSO structure, as the diffraction spots evenly divided the distance between the incident beam and the $(0002)_\alpha$ diffraction spots into 14 sections. The fine particles were distributed along the grain boundaries, as shown in Fig. 5b, which, according to the SAED pattern, can be identified as the Mg_5RE phase ($F\bar{4}3m$, a = 2.2 nm) [35]. Table 1 summarizes the volume fractions of various phases in each state sample. The hot extrusion at a higher extrusion ratio resulted in a lower volume fraction of the Mg_5RE phase. However, the extrusion ratio had a negligible effect on the LPSO phase, as the comparable volume fraction of the LPSO phase achieved in samples E6 and E30 was 7.0 ± 0.5 and 7.3 ± 1.3%, respectively.

The EBSD inverse pole figure (IPF) maps and the corresponding IPFs of samples E6 and E30 are shown

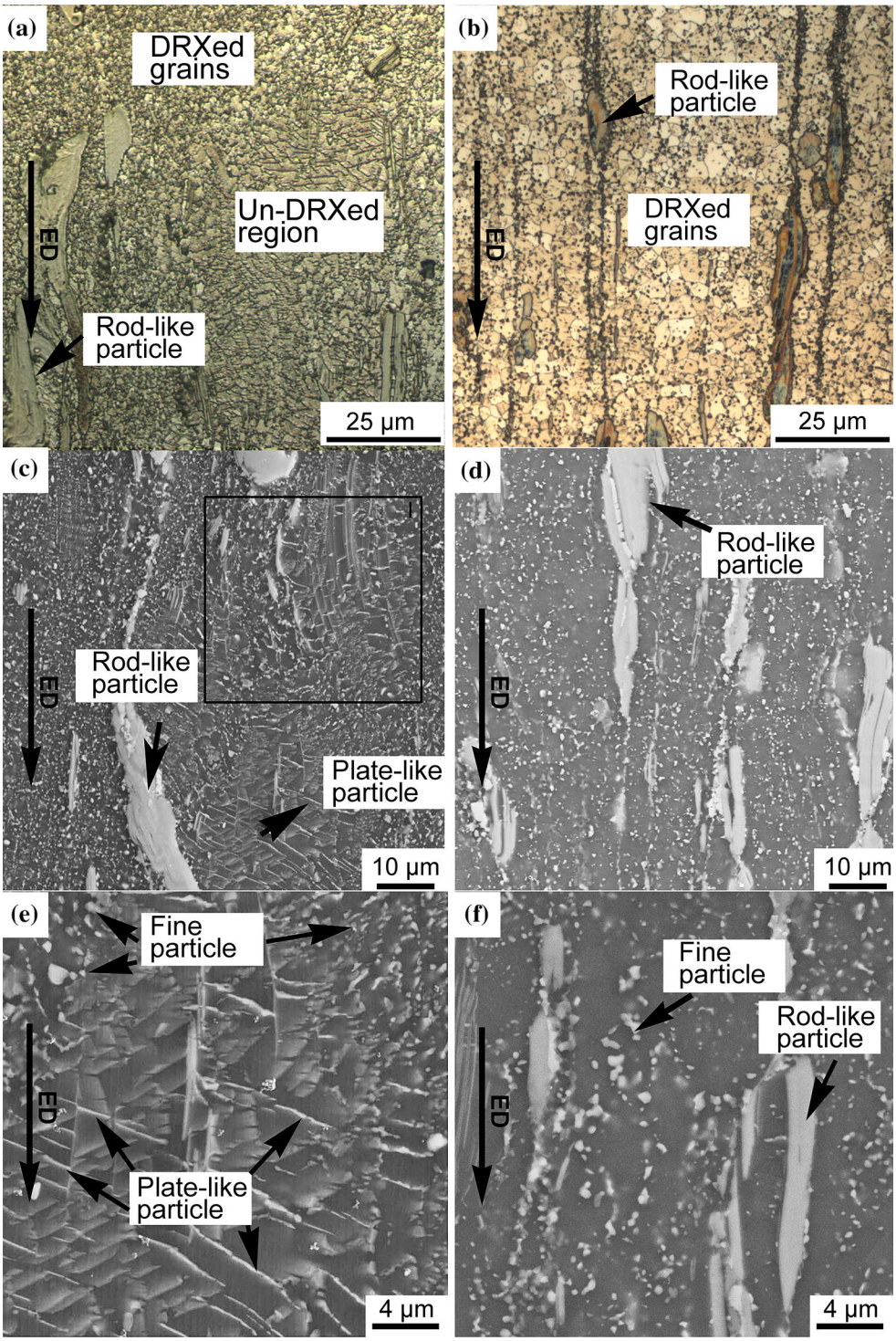

Figure 2 OM and SEM images of samples, **a**, **c**, **e** E6, **b**, **d**, **f** E30.

in Fig. 6a–f. The small black spot and large black regions in the IPF maps are caused by the existence of the Mg_5RE particles and the LPSO particles, respectively. Figure 6a, c shows that after the hot extrusion, samples E6 and E30 had significantly different microstructures. Sample E6 exhibited a bimodal structure consisting of DRXed grains and un-DRXed regions (Fig. 6a). Several low-angle grain boundaries (LAGBs) with misorientation angles below 15° were formed in the un-DRXed regions and resulted in

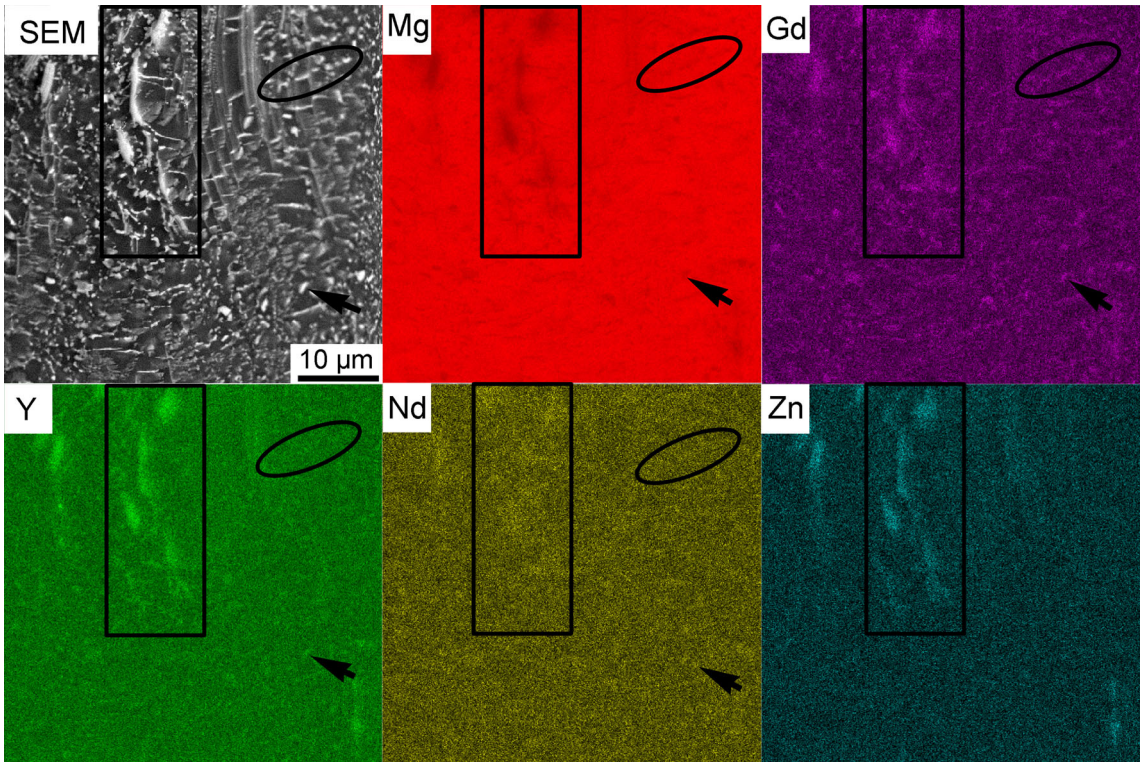

Figure 3 SEM image and corresponding EDS elemental mappings recorded from the *highlighted* region I in Fig. 2c.

subgrain structures (Fig. 6b). Compared with sample E6, sample E30 exhibited a homogeneous structure consisting of DRXed grains (Fig. 6c). The local textures were shown using IPFs obtained by EBSD measurements. The regions, from which the IPFs were measured, are shown in Fig. 6a, c, e. Samples E6 and E30 exhibited a bimodal texture having [0001] and <10$\bar{1}$0> texture components, i.e. most grains were orientated with the [0001] and <10$\bar{1}$0> parallel to the ED (Fig. 6b, f). The un-DRXed regions in sample E6 had a very strong texture and were orientated with the <10$\bar{1}$0> parallel to the ED (Fig. 6d). Figure 7a shows the grain size distributions of samples E6 and E30. Sample E6 exhibited a bimodal microstructure via the discontinuous grain size distribution. Most of the DRXed grains had a size smaller than 3 μm, whereas a few un-DRXed grains had a size greater than 9 μm. In contrast, sample E30 exhibited a homogeneous microstructure having a continuous grain size distribution. The average DRXed grain sizes for samples E6 and E30 were 1.6 ± 0.6 and 3.6 ± 1.2 μm, respectively (Table 1). Figure 7b shows the quantitative analysis of the misorientation angle distribution for samples E6 and E30. The fraction of LAGBs was significantly decreased with the larger extrusion ratio, indicating that the higher extrusion ratio promotes the DRX process and reduces the un-DRXed regions.

Microstructure after annealing treatments

Figure 8 shows the microstructures of samples E6 and E30 after the annealing treatments at 450 °C for 24 and 72 h. The figure shows that most of the Mg_5RE

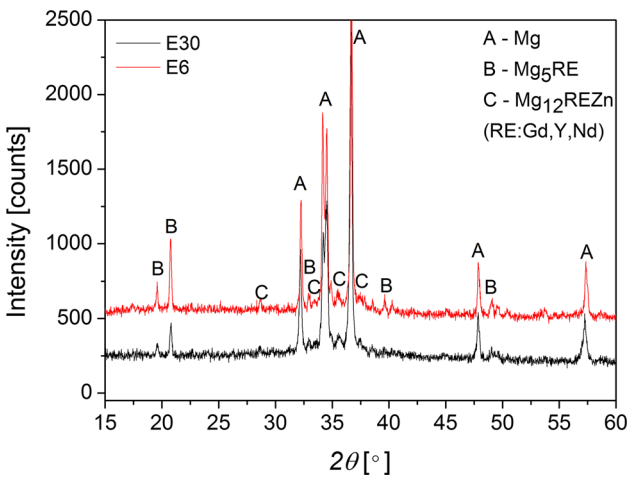

Figure 4 X-ray diffraction patterns of samples E6 and E30.

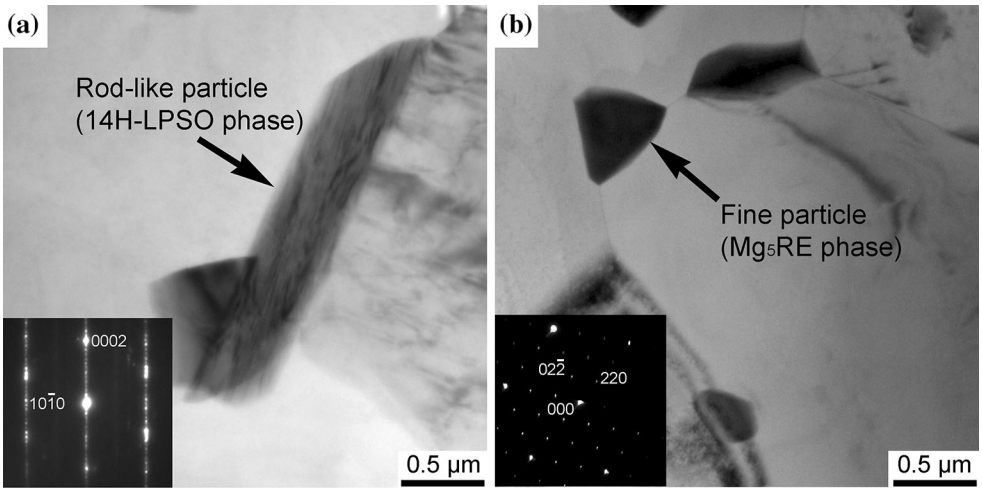

Figure 5 TEM images and corresponding SAED patterns of **a** LPSO phase and **b** Mg_5RE phase.

Table 1 Volume fractions of the various types of phases in each sample

Samples	Volume fraction (%)			Grain size (μm)
	Mg_5RE phase	LPSO phase	Cuboid phase	
E6	9.3 ± 0.7	7.0 ± 0.5	–	1.6 ± 0.6
E30	6.6 ± 0.4	7.3 ± 1.3	–	3.6 ± 1.2
E6A1	7.5 ± 0.8	6.3 ± 1.0	0.2 ± 0.1	6.5 ± 1.4
E30A1	5.6 ± 0.5	7.7 ± 0.7	–	8.1 ± 1.1
E6A2	6.6 ± 0.9	6.7 ± 1.1	0.3 ± 0.1	7.8 ± 1.0
E30A2	2.4 ± 0.6	7.6 ± 1.7	–	12.8 ± 1.5

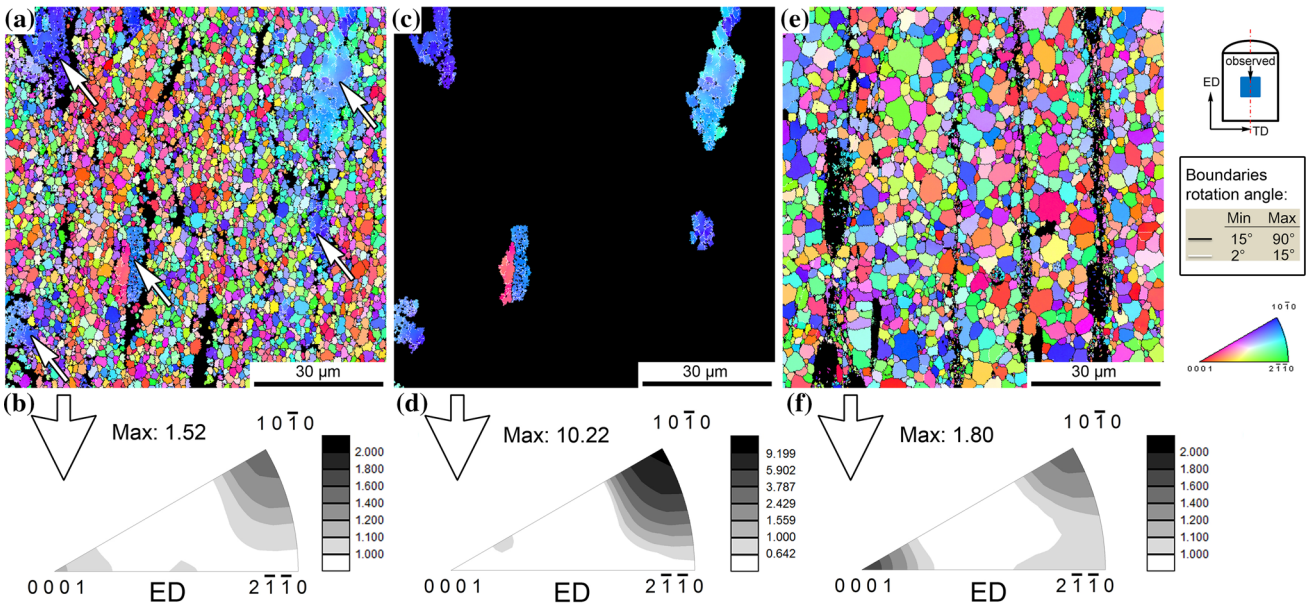

Figure 6 EBSD IPF maps and corresponding IPFs for samples E6 and E30: **a**, **b** all grains, **c**, **d** un-DRXed regions in sample E6 and **e**, **f** all grains in sample E30.

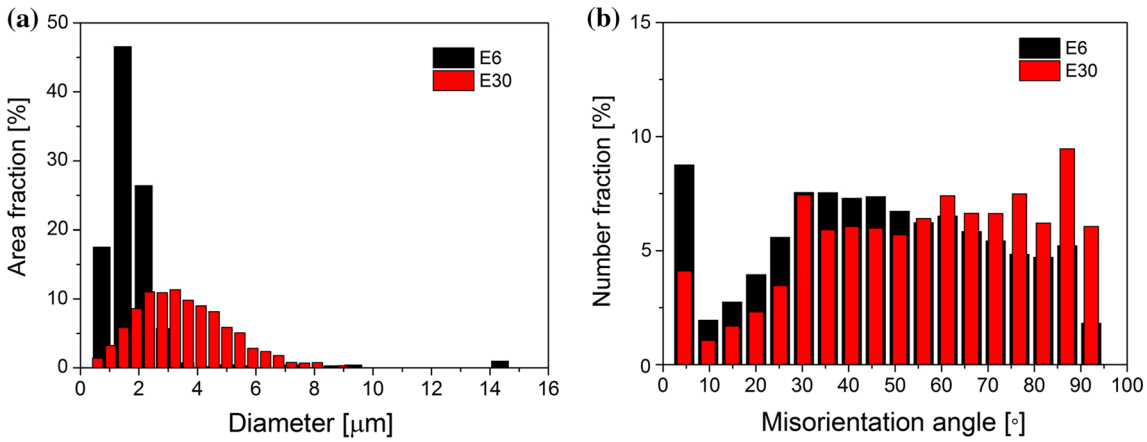

Figure 7 **a** Grain size distribution diagram and **b** misorientation angle of samples E6 and E30.

particles were dissolved into the matrix during annealing. In contrast, there were almost no changes in the morphology and volume fraction of the LPSO particles. The volume fraction of the Mg_5RE particles decreased to 7.5 ± 0.8 and 5.6 ± 0.5% for samples E6A1 and E30A1 after annealing for 24 h and further decreased to 6.6 ± 0.9 and 2.4 ± 0.6% for samples E6A2 and E30A2 after annealing for 72 h,

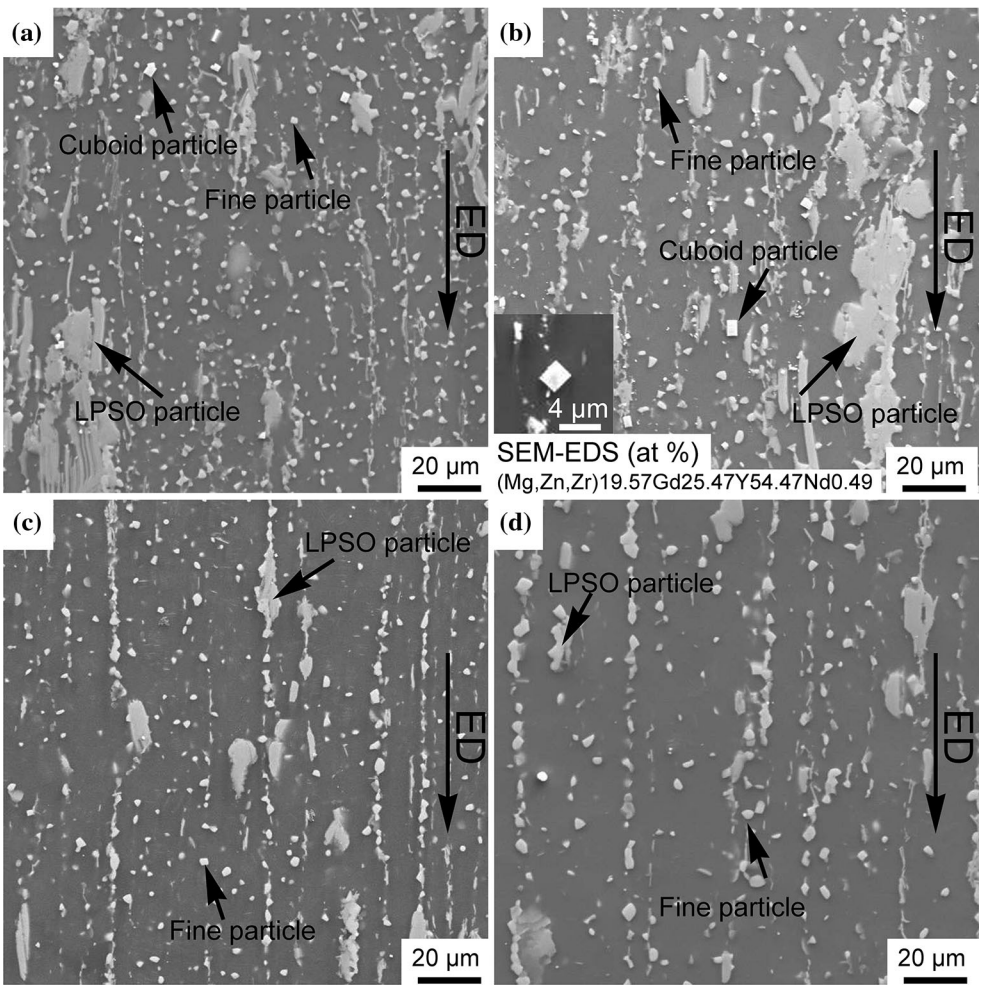

Figure 8 SEM images of samples, **a** E6A1, **b** E6A2, **c** E30A1 and **d** E30A2.

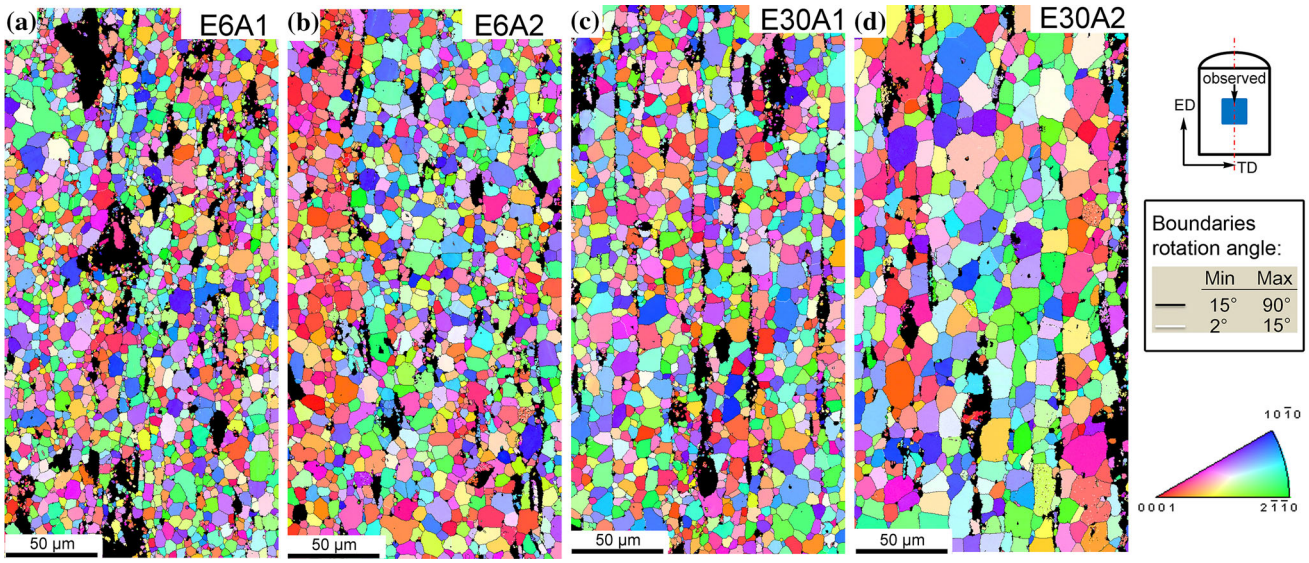

Figure 9 EBSD IPF maps of samples E6 and E30 after the annealing treatments: **a** E6A1, **b** E6A2, **c** E30A1 and **d** E30A2.

respectively (Table 1). Although the Mg_5RE particles underwent dissolution during annealing, the samples with a low extrusion ratio (E6A1 and E6A2) still had a higher volume fraction of Mg_5RE particles than that of samples with a high extrusion ratio (E30A1 and E30A2). Note that some cuboid particles of approximately 2 μm in diameter formed on samples E6A1 and E6A2 (Fig. 8a, b). The SEM–EDS results indicate that these cuboid particles are rich in Gd, Y and Nd. However, these cuboid RE-rich particles were not observed in samples E30A1 and E30A2 (Fig. 8c, d). The volume fractions of these cuboid particles were less than 1% in both the E6A1 and E6A2 samples (Table 1). Static recrystallization occurred in sample E6 during annealing. As a result, the large un-DRXed regions were eventually replaced by the recrystallized grains after annealing for 24 h. Due to the continuous dissolution, the plate-like Mg_5RE particles eventually disappeared. The homogeneity of the precipitate distribution was also promoted with the prolonged annealing time. The EBSD IPF maps (Fig. 9) show the microstructures after the annealing treatments. The annealed samples consisted entirely of recrystallized grains, and there was limited abnormal grain growth observed. The average grain sizes varied depending on the extrusion ratio and annealing time (Table 1). Samples E6A1 and E6A2 had an average grain size of 6.5 ± 1.4 and 7.8 ± 1.0 μm, respectively, whereas samples E30A1 and E30A2 had an average grain size of 8.1 ± 1.1 and 12.8 ± 1.5 μm, respectively. The high extrusion ratio and long-term annealing resulted in a larger grain size, which could be related to the volume fraction of the Mg_5RE particles in the annealed samples.

Textures

The effects of the extrusion ratio and annealing treatment on the textures were determined by EBSD and synchrotron radiation measurements. The local textures were presented using IPFs obtained with the EBSD measurements (Fig. 10a, b). It can be seen that samples E6 and E30 exhibited a bimodal texture consisting of <0001> and <10$\bar{1}$0> components. Additional IPFs were measured separately depending on the grain size in the same regions. The <0001> texture component was not evident until the grain size exceeded a critical value, which was 2.0 μm for sample E6 and 2.3 μm for sample E30. After annealing the samples for 24 h, the texture components remained unchanged (Fig. 10c, d), while after annealing the samples for 72 h, the <11$\bar{2}$0> texture component was newly formed in both the E6A2 and E30A2 samples (Fig. 10e, f). The annealed samples, like the extruded one, provided critical grain sizes for the appearance of the <0001> texture. These critical grain sizes were 2.9 and 4.7 μm for samples

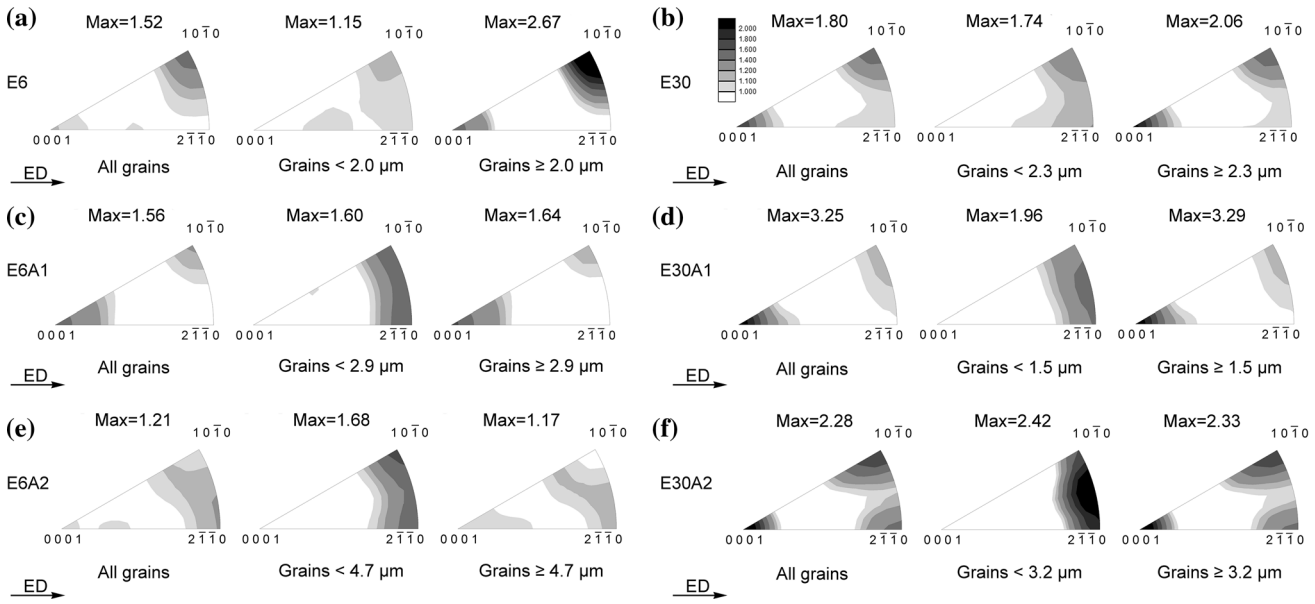

Figure 10 IPFs of samples E6 and E30 before and after the annealing treatments: **a** E6, **b** E30, **c** E6A1, **d** E30A1, **e** E6A2 and **f** E30A2. *Note* the IPFs are also presented depending on the critical grain size for each sample.

E6A1 and E6A2, and 1.5 and 3.2 μm for samples E30A1 and E30A2, respectively.

The macro-textures were observed after using the (0001) and {10$\bar{1}$0} pole figures (PFs) obtained by the synchrotron radiation measurements (Fig. 11). Sample E6 exhibited a macro-texture with the {11$\bar{2}$0}<10$\bar{1}$0> component. The strong intensity peaks (green circles) spread towards the transverse direction (TD) in the (0001) PF and towards the ED in the {10$\bar{1}$0} PF (Fig. 11a). The appearance of additional intensity peaks in the centre of the (0001) PF indicates that an extra (0001) <10$\bar{1}$0> component existed in sample E6. For sample E30, in addition to the {11$\bar{2}$0}<10$\bar{1}$0> component, as indicated by the green circles in Fig. 11d, another <10$\bar{1}$0> fibre component was present. In addition, a weak {11$\bar{2}$0}<0001> texture component, which is highlighted by blue circles in the (0001) and {10$\bar{1}$0}PFs, was also observed. Unlike the IPFs obtained by the EBSD measurements, the PFs obtained by the synchrotron measurements show that no <0001> texture component existed in samples E6, E6A1 or E6A2 (Fig. 11a–c). However, it is evident that the <0001> texture component existed in samples E30, E30A1 and E30A2 due to the appearance of the orientation girdle in the {10$\bar{1}$0} PFs (Fig. 11d–f). In general, the <0001> texture in the IPF corresponds to the {11$\bar{2}$0} [0001] component and the <0001> fibre component in the PF. The <10$\bar{1}$0> texture in the IPF corresponds to the <10$\bar{1}$0> fibre component and the {11$\bar{2}$0}<10$\bar{1}$0> component in the PF.

Mechanical properties

Table 2 summarizes the mechanical properties of various samples. Sample E6 exhibited a higher ultimate tensile strength (UTS) and a YS but a lower elongation to failure compared with sample E30. The UTS, YS and elongation to failure were 377 ± 7.4, 342 ± 8.0 MPa and 3.2 ± 0.9%, respectively, for sample E6, and 363 ± 3.2, 306 ± 1.0 MPa and 6.2 ± 0.9%, respectively, for sample E30. After annealing the samples for 24 h, the UTS and YS largely decreased for both of the samples, while their elongation to failure varied differently. The elongation to failure increased to 5.2 ± 0.4% for sample E6A1, while it slightly decreased to 6.0 ± 0.8% for sample E30A1. After annealing the samples for 72 h, the UTS and YS further decreased to 292 ± 4.0 and 224 ± 6.3 MPa for sample E6A2 and to 296 ± 3.2 and 243 ± 1.7 MPa for sample E30A2, respectively. The elongation to failure slightly increased to 5.8 ± 0.7% for sample E6A2 and to 6.2 ± 0.8% for sample E30A2.

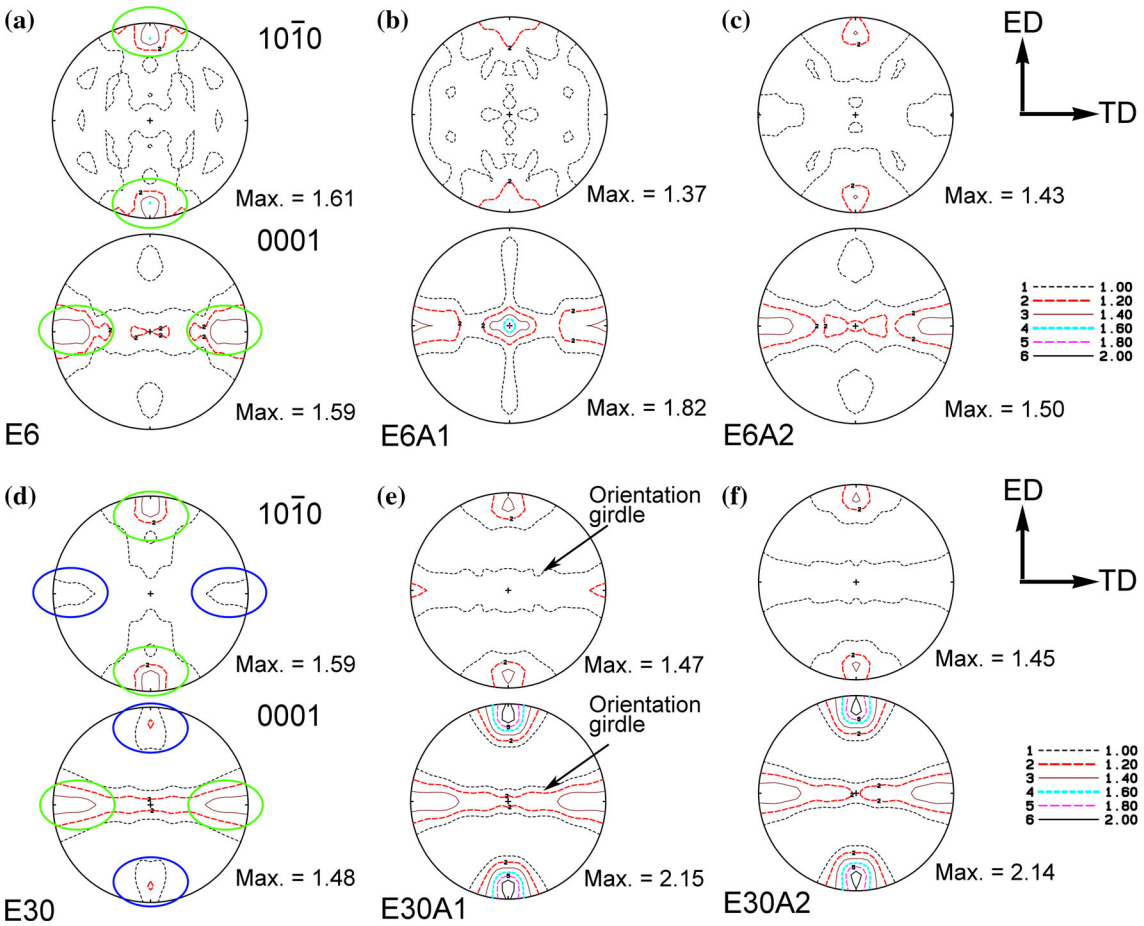

Figure 11 PFs of samples E6 and E30 before and after the annealing treatments measured with synchrotron radiation diffraction: **a** E6, **b** E6A1, **c** E6A2, **d** E30, **e** E30A1 and **f** E30A2.

Discussion

Microstructural evolution

Role of the extrusion ratio

The extrusion ratio has significant effects on the microstructural evolution of the samples by generating differences in the microstructural homogeneity and the particle distribution. The low extrusion ratio (6:1) leads to a bimodal microstructure consisting of DRXed grains and un-DRXed regions. In contrast, the high extrusion ratio (30:1) leads to a homogeneous microstructure consisting of only of DRXed grains. The extent of dynamic recrystallization increases as the extrusion ratio increases. Similar results were also reported in previous investigations [2, 7–9]. In those investigations, two critical strains were seriously considered for the dynamic recrystallization [7, 8]. The first critical strain is required to trigger the dynamic recrystallization, and the second one

Table 2 Tensile mechanical properties at room temperature

Samples	0.2% proof strength (MPa)	Ultimate tensile strength (MPa)	Elongation to failure (%)
E6	342 ± 8.0	377 ± 7.4	3.2 ± 0.9
E6A1	232 ± 4.3	311 ± 3.5	5.2 ± 0.4
E6A2	224 ± 6.3	292 ± 4.0	5.8 ± 0.7
E30	306 ± 1.0	363 ± 3.2	6.2 ± 0.9
E30A1	253 ± 6.0	307 ± 3.3	6.0 ± 0.8
E30A2	243 ± 1.7	296 ± 3.2	6.2 ± 0.8

determines the degree of microstructural homogeneity. Considering that the studied alloy has undergone dynamic recrystallization with either high or low extrusion ratios, the second critical strain primarily concerns the microstructural homogeneity. The applied extrusion strains are 1.8 and 3.4 for samples E6 and E30, respectively. It is evident that strains larger than the second critical strain of the studied alloy of 3.4 are sufficient to achieve a homogeneous microstructure with fine DRXed grains.

The studied alloy contains several particles, such as Mg_5RE and LPSO particles. Due to the high thermal stability of the LPSO phase, it is not prone to dissolution into the matrix during the preheating treatment and hot extrusion [6]. Shao et al. [36] reported that the LPSO particles have a greater hardness than that of the Mg matrix. The dense distribution of the LPSO particles can efficiently prevent the Mg matrix from severely deforming by withstanding greater external stress. Thus, in the alloy extrusion with a low extrusion strain, i.e. sample E6, the regions close to the LPSO particles are subject to an insufficient local deformation. Consequently, partial recrystallization occurs (Fig. 2c). In sample E30, despite the resistance effects of the LPSO particles on dynamic recrystallization, a large extrusion strain results in the completed recrystallization (Fig. 2d).

In addition to the LPSO particles, plate-like particles were observed in the un-DRXed regions of sample E6, while they were scarcely observed in sample E30. Our previous investigation revealed that the plate-like Mg_5RE particles are formed during the preheat treatment [6]. The particles could transform into globular particles by cracking and spheroidization in the subsequent hot extrusion process. In this process, severe plastic deformation is necessary to crush the plate-like particles. In sample E6, due to the low extrusion strain and the insufficient local deformation near the LPSO particles, these plate-like particles cannot successfully transform into globular particles and their original morphology is preserved in the un-DRXed regions.

The extruded alloys exhibit a refined microstructure with an average DRXed grain size of 1.6 ± 0.6 μm for sample E6 and 3.6 ± 1.2 μm for sample E30. Hantzsche et al. [37] suggested that the restricted grain growth for the Mg–RE alloys is attributed to the grain boundary pinning effect caused by solute segregation and the particles that are present. Stanford [38] confirmed that the strong interactions among the RE solutes, dislocations and grain boundaries are responsible for the significant grain refinements. Nevertheless, Stanford and Callaghan [39] revealed that the addition of the RE elements induces a higher stored energy and promotes the DRX process, thereby resulting in grain refinement. Thus, it is reasonable that the addition of RE elements contributes to the grain refinement for the studied alloy. In addition, the high RE content induces a high volume fraction of the second phase particles. The volume fractions of the Mg_5RE and LPSO phase particles are 9.3 and 7% in sample E6, and 6.7 and 7.6% in sample E30, respectively. The extrusion ratio has a significant effect on the volume fraction of the Mg_5RE phase but has a limited effect on the LPSO phase. This difference might result from the different characteristics of these phases. Compared with the Mg_5RE phase, the LPSO phase has better thermal stability [24]. As a result, sample E6 has a higher volume fraction of the Mg_5RE phase compared with sample E30. Because there is a dense distribution of the Mg_5RE phase particles at the grain boundaries, their pinning effect plays an important role in the grain refinement [9, 37]. The higher volume fraction of the Mg_5RE phase results in a finer DRXed grain size in sample E6. In contrast, the lower volume fraction of the Mg_5RE phase leads to a larger DRXed grain size in sample E30.

Samples E6 and E30 exhibit a weak bimodal texture with the $<10\bar{1}0>$ and $<0001>$ components. The maximum texture intensity for sample E6 was a 1.52 multiple of random distribution (M.R.D) obtained by the EBSD measurement and a 1.61 M.R.D obtained by the synchrotron radiation measurement. These values were 1.80 M.R.D (EBSD measurement) and 1.59 M.R.D (synchrotron radiation measurement) for sample E30. It was reported that the RE additions efficiently weaken the texture due to the strong interactions among the RE solutes, dislocations and grain boundaries [30, 40]. However, the texture intensity decreases with the increasing volume fraction of the second phase particles [41]. Considering the high RE content and large number of second phase particles, the texture weakening is expected in the studied alloy.

The $<10\bar{1}0>$ texture is commonly observed in extruded Mg alloys. The formation of this texture is attributed to the activation of twins and basal slip at an early stage of the extrusion [28, 42]. In addition to

the weak <10$\bar{1}$0> texture component, an additional <0001> texture component was observed in samples E6 and E30 (Fig. 10a, b). This <0001> texture component was previously reported in Mg–RE alloys extruded with high extrusion ratios in the range of 17:1–19:1 [2, 3]. However, even though the studied alloy was extruded with a low extrusion ratio of 6:1, the <0001> texture component was still observed. In addition, the present results reveal that the appearance of the <0001> texture component is determined by a critical grain size, whereas the appearance of <10$\bar{1}$0> texture component is independent of the grain size, indicating that the formation of the <0001> texture component is largely related to the grain growth rather than the extrusion ratio. These textural grains have a preferential growth in the <0001> orientation during the hot extrusion. The extrusion ratio mainly contributes to the recrystallization process. As previously mentioned, the solute segregation and particle pinning at the grain boundaries significantly influence the grain growth. Robson et al. [2] revealed that the <0001> texture component originated from the recrystallized grains, which have a preferential growth over other grains. Alizadeh et al. [3] suggested that the solute drag of the RE elements and the retarding effects of the second phase particles are the main mechanisms responsible for the formation of the <0001> texture component. The solute segregation to the grain boundaries and the slow diffusion rate of the solute atoms may promote the growth of certain orientations. Considering the high RE content and high volume fraction of the second phase particles in the studied alloy, the <0001> texture component can be successfully produced at a low extrusion ratio of 6:1.

Role of the annealing treatment

Compared with sample E6, samples E6A1 and E6A2 exhibit a homogeneous microstructure with the DRXed grains rather than a bimodal microstructure with the un-DRXed regions and DRXed grains. This microstructural evolution is attributed to the static recrystallization during the annealing treatment. The stored energy associated with the residual strain in the un-DRXed regions acts as a driving force and activates the static recrystallization as normal grain growth rather than abnormal grain growth. The important factors influencing the grain growth include the second phase particles and the texture [32]. The as-extruded alloy primarily contains the LPSO and Mg_5RE particles. As previously mentioned, the existence of the LPSO particles results in un-DRXed regions at the low extrusion ratio, thereby providing the requisite microstructure for static recrystallization. The thermally stable LPSO phase particles provide impassable Mg/LPSO interfaces against which the neighbouring grains grow. Therefore, the neighbouring grains must grow towards free regions of the LPSO phase particles. The Mg_5RE phase particles resist the grain growth by pinning at grain boundaries. Due to the continuous dissolution during annealing, the pinning effect is gradually reduced, resulting in grain coarsening. The volume fraction of the Mg_5RE phase particles for samples E6A1, E6A2, E30A1 and E30A2 is 7.5 ± 0.8, 6.6 ± 0.9, 5.6 ± 0.5 and 2.4 ± 0.9%, respectively, and the grain sizes are 6.5 ± 1.4, 7.8 ± 1.0, 8.1 ± 1.1 and 12.8 ± 1.5 μm, respectively (Table 1). The higher volume fraction of the Mg_5RE phase results in a finer grain size after annealing. Due to the comparable volume fractions of the LPSO phase in samples E6 and E30 both before and after annealing, the present grain growth during annealing is largely determined by the Mg_5RE phase rather than the LPSO phase.

Some cuboid RE-rich particles were observed in samples E6A1 and E6A2, which were not found in samples E6, E30, E30A1 and E30A2 (Figs. 2, 8). This cuboid phase was previously reported in Mg–Gd–Y-based alloys [3, 43, 44], and its formation was a result of the dissolution of the Mg_5RE phase [44]. In this dynamical and continuous dissolution procedure, the network-like Mg_5RE phase was transformed to a spheroidized Mg_5RE phase and a cuboid RE-rich phase. Finally, the spheroidized Mg_5RE phase was completely dissolved, whereas the cuboid RE-rich phase remained. In the present work, sample E6 retains several plate-like Mg_5RE phase particles in the un-DRXed regions (Fig. 2e), which provide appropriate nucleation sites for the cuboid RE-rich phase in the subsequent annealing treatments. Thus, the cuboid RE-rich particles can be observed in samples E6A1 and E6A2. Due to the absence of plate-like Mg_5RE phase particles, the cuboid phase is rarely observed in sample E30 after the annealing treatments. It is evident that the fine Mg_5RE phase cannot lead to the formation of the cuboid phase; otherwise, the phase constitution should be the same in samples E6 and E30 after annealing.

Texture is another factor that influences the grain growth, and the grain growth influences the texture evolution, including its intensity and components [26, 33, 45, 46]. It was reported that a short-term annealing at a moderate temperature leads only to small changes in the texture [26, 45]. The strengthening of the texture components normally results from a normal grain growth. In the studied alloy, remarkable changes in the texture components were not observed after annealing at 450 °C for 24 h (Fig. 10b, c). With prolonged annealing to 72 h, a new <11$\bar{2}$0> texture component became visible (Fig. 10e, f). Pérez-Prado et al. [26] reported that the abnormal grain growth can cause a new texture component. Yi et al. [47] confirmed that the dominant texture component changes from the previous <10$\bar{1}$0> to the newly formed <11$\bar{2}$0> component due to the preferential growth of the <11$\bar{2}$0> textural grains during a long-term annealing process. The studied alloy exhibited a suppressed abnormal grain growth during annealing due to the grain boundary pinning by the second phase particles. However, the grains are coarsened as a result of the continuous reduction in the volume fraction of the Mg_5RE phase. Because the grains have a preferential growth in the <11$\bar{2}$0> orientation, the <11$\bar{2}$0> texture component eventually becomes visible after annealing for 72 h. The present results show that the texture components are produced depending on the annealing time, i.e. the degree of grain growth, which is related to the dissolution of the Mg_5RE particles.

Microstructures and strengthening

The strengthening of the Mg alloys is primarily attributed to grain refinement, texture and second phase particles [4, 31, 48]. In sample E30, the average grain size is only 3.6 ± 1.2 μm. These fine grains lead to a high YS. Due to the coexistence of the DRXed and un-DRXed regions, it is difficult to determine the average grain size for sample E6. However, the average grain size in the DRXed regions can be evaluated as 1.6 ± 0.6 μm. Therefore, the fine DRXed grains improve the YS of sample E6 to some extent.

The texture should be another contributor to the strengthening of the studied alloy. A weak texture with <10$\bar{1}$0> and <0001> components parallel to the ED was observed in samples E6 and E30. The <0001> texture component assists the activation of tensile twinning, thereby reducing the YS when a tensile load is applied in the <0001> orientation. Our previous investigation revealed that the tensile twins are less pronounced in the studied alloy at the initial stage of the tensile deformation [49]. The low twinning activity is attributed to the fine grains [50], and while the <0001> component is beneficial for the twin activation, it cannot lead to a large reduction in the YS due to the fine grains. In contrast, a further increase in the YS can be expected because most of the grains have the <10$\bar{1}$0> or <0001> orientations parallel to the ED. These grains have a negligible Schmid factor for basal slip.

The existence of several second phase particles also contributes to the strengthening of the studied alloy (Table 1). Hagihara et al. [21, 23] observed that the $(0001)_{LPSO}$ is parallel to the layered interface of the LPSO phase. The authors suggested that the (0001) <11$\bar{2}$0> basal slip is the dominant operative deformation mode in the LPSO phase. As the layered interface is parallel to the ED, the tensile load is applied in a hard orientation for the basal slip in the LPSO phase. The deformation is suppressed until the tensile load is sufficiently high to activate the other slip systems in the LPSO phase. Thus, the aligned LPSO phase particles act as reinforcements to strengthen the alloy through short-fibre strengthening [21]. In addition, the fine Mg_5RE particles could provide additional dispersion strengthening [24, 48].

In the present study, the different extrusion ratios give rise to different mechanical performances. Sample E6 exhibits a raised YS but a lowered elongation to failure compared with sample E30. The different mechanical behaviours are ascribed to the differences in their microstructures. First, sample E6 shows a bimodal microstructure consisting of fine DRXed grains with an average grain size of 1.6 ± 0.6 μm and course un-DRXed grains containing plate-like particles. Sample E30 shows a fully recrystallized microstructure with an average grain size of 3.6 ± 1.2 μm. The smaller DRXed grains lead to a higher YS for sample E6. The plate-like particles contribute to not only the precipitation hardening but also the suppression of the deformation twinning in the coarse un-DRXed grains [51]. The strong <10$\bar{1}$0> texture of these coarse un-DRXed grains also provides a hard orientation for the basal slip and twinning deformation. Therefore, a high YS and a low elongation to failure can be expected for

sample E6. Second, the volume fractions of the Mg_5RE phase are 9.3 and 6.7% for samples E6 and E30, respectively. Although these fine particles strengthen the alloy via the dispersion strengthening mechanism, they provide a path for crack propagations at grain boundaries and reduce the alloy ductility [6]. Therefore, the higher volume fractions of the Mg_5RE phase particles in sample E6 increase the YS but decrease the elongation to failure.

After annealing the samples at 450 °C, the YS is reduced for each sample (Table 2). The annealing treatments increase the grain size, thus weakening the grain boundary strengthening. Due to the grain size dependence of the twinning activity, the coarsened grains improve the twinning activity [50]. Under these circumstances, the coarsened grains oriented along the [0001] parallel to the ED lead to a further decrease in the YS. In addition, the dispersion strengthening is also reduced due to the decreased volume fraction of the Mg_5RE phase after annealing. Although the cuboid RE-rich phase is newly formed in samples E6A1 and E6A2, it might not significantly contribute to the mechanical properties due to its limited volume fraction. The annealing treatments not only affect the strength but also influence the ductility, especially for sample E6 (Table 2). The annealing treatment increases the elongation to failure by approximately 2% for sample E6A1. With the prolonged annealing, the elongation to failure is only increased by approximately 0.6% for sample E6A2. The large improvement in the ductility for sample E6A1 is attributed to the disappearance of the bimodal microstructure. In addition, the decrease in the volume fraction of the Mg_5RE phase also contributes to the improvement in the ductility.

Conclusions

This study investigated the effects of the extrusion ratio and annealing treatment on the microstructure, texture and mechanical properties of an as-extruded Mg–11Gd–4.5Y–1Nd–1.5Zn–0.5Zr (wt%) alloy. The following conclusions are obtained:

1. An extruded Mg bar with a high strength is successfully produced. The Mg bar exhibits a YS of 342 ± 8.0 MPa and an elongation to failure of 3.2 ± 0.9%. After the annealing treatment at 450 °C for 72 h, the YS was reduced to 224 ± 6.3 MPa, and the elongation to failure increased to 5.8 ± 0.7%.
2. The extrusion ratio affects the microstructural homogeneity. The low extrusion ratio (6:1) results in a bimodal microstructure with fine DRXed grains and coarse un-DRXed grains, while the high extrusion ratio (30:1) results in a homogeneous microstructure with fine DRXed grains.
3. The volume fraction of the Mg_5RE phase decreases as the extrusion ratio and annealing time increase. The extrusion ratio and annealing treatment have negligible effects on the volume fraction of the LPSO phase. The annealing treatment not only removes the bimodal microstructures but also induces the cuboid RE-rich phase in sample E6. Grain growth during annealing is controlled by the Mg_5RE phase rather than the LPSO phase.
4. The extruded alloy exhibits a bimodal texture with <0001> and <10$\bar{1}$0> components. The presence of the <0001> texture component is determined by a critical grain size. The extrusion ratio has limited effect on the texture with respect to its component and intensity. The texture evolution during annealing depends on the annealing time, i.e. the degree of grain growth.
5. The alloy strengthening is attributed to the grain refinement, the Mg_5RE and LPSO phases, and the texture.

Acknowledgements

The authors thank Ms. Yuling Xu for her assistance with the data analysis. This work is supported by the National Key Technologies R&D Program (2012BAE 01B04, 2012DFH50100, KGFZD-125-13-021, 201001C0 104669453). Zijian Yu would like to thank the Chinese Academy of Sciences and the German Academic Exchange Service (CAS-DAAD) scholarship programme for their financial support.

Compliance with ethical standards

Conflict of interest The authors declare that they have no conflict of interest.

References

[1] Mordike BL, Ebert T (2001) Magnesium: properties—applications—potential. Mater Sci Eng A 302:37–45

[2] Robson JD, Twier AM, Lorimer GW, Rogers P (2011) Effect of extrusion conditions on microstructure, texture, and yield asymmetry in Mg–6Y–7Gd–0.5 wt%Zr alloy. Mater Sci Eng A 528:7247–7256

[3] Alizadeh R, Mahmudi R, Ngan AHW, Langdon TG (2016) An unusual extrusion texture in Mg–Gd–Y–Zr alloys. Adv Eng Mater 18:1044–1049

[4] Homma T, Kunito N, Kamado S (2009) Fabrication of extraordinary high-strength magnesium alloy by hot extrusion. Scr Mater 61:644–647

[5] Yamasaki M, Anan T, Yoshimoto S, Kawamura Y (2005) Mechanical properties of warm-extruded Mg–Zn–Gd alloy with coherent 14H long periodic stacking ordered structure precipitate. Scr Mater 53:799–803

[6] Yu Z, Huang Y, Mendis CL, Hort N, Meng J (2015) Microstructural evolution and mechanical properties of Mg–11Gd–4.5Y–1Nd–1.5Zn–0.5Zr alloy prepared via pre-ageing and hot extrusion. Mater Sci Eng A 624:23–31

[7] Chen Y, Wang Q, Peng J, Zhai C, Ding W (2007) Effects of extrusion ratio on the microstructure and mechanical properties of AZ31 Mg alloy. J Mater Process Technol 182:281–285

[8] Shahzad M, Wagner L (2009) Influence of extrusion parameters on microstructure and texture developments, and their effects on mechanical properties of the magnesium alloy AZ80. Mater Sci Eng A 506:141–147

[9] Roy S, Kannan G, Suwas S, Surappa MK (2015) Effect of extrusion ratio on the microstructure, texture and mechanical properties of (Mg/AZ91)m–SiCp composite. Mater Sci Eng A 624:279–290

[10] Sadeghi A, Pekguleryuz M (2012) Effect of pre-deformation anneal on the microstructure and texture evolution of Mg–3Al–1Zn–0.7Sr alloy during hot extrusion. J Mater Sci 47:5374–5384. doi:10.1007/s10853-012-6416-0

[11] Mordike BL (2002) Creep-resistant magnesium alloys. Mater Sci Eng A 324:103–112

[12] Rokhlin LL (2003) Rokhlin magnesium alloys containing rare earth metals: structure and properties. Taylor & Francis Ltd, London, pp 1–256

[13] Wen K, Du W-B, Liu K, Wang Z-H, Li S-B (2016) Microstructures and mechanical properties of homogenization and isothermal aging Mg–Gd–Er–Zn–Zr alloy. Rare Met 35:443–449

[14] Xu C, Zheng MY, Wu K, Wang ED, Fan GH, Xu SW, Kamado S, Liu XD, Wang GJ, Lv XY, Li MJ, Liu YT (2013) Effect of final rolling reduction on the microstructure and mechanical properties of Mg–Gd–Y–Zn–Zr alloy sheets. Mater Sci Eng A 559:232–240

[15] Yu D, Zhang D, Sun J, Luo Y, Xu J, Zhang H, Pan F (2017) Improving mechanical properties of ZM61 magnesium alloy by aging before extrusion. J Alloys Compd 690:553–560

[16] Lin L, Chen L, Liu Z (2008) Tensile strength improvement of an Mg–12Gd–3Y (wt%) alloy processed by hot extrusion and free forging. J Mater Sci 43:4493. doi:10.1007/s10853-008-2650-x

[17] Lu JW, Yin DD, Ren LB, Quan GF (2016) Tensile and compressive deformation behavior of peak-aged cast Mg–11Y–5Gd–2Zn–0.5Zr (wt%) alloy at elevated temperatures. J Mater Sci 51:10464–10477. doi:10.1007/s10853-016-0266-0

[18] Massalski TB, Okamoto H (1990) Binary alloy phase diagrams. ASM International, Materials Park

[19] Peng Q, Wu Y, Fang D, Meng J, Wang L (2007) Microstructures and mechanical properties of Mg–8Gd–0.6Zr–xNd ($x = 0$, 1, 2 and 3 mass%) alloys. J Mater Sci 42:3908–3913. doi:10.1007/s10853-006-0451-7

[20] Penghuai F, Liming P, Haiyan J, Lan M, Chunquan Z (2008) Chemical composition optimization of gravity cast Mg–yNd–xZn–Zr alloy. Mater Sci Eng A 496:177–188

[21] Hagihara K, Kinoshita A, Sugino Y, Yamasaki M, Kawamura Y, Yasuda HY, Umakoshi Y (2010) Effect of long-period stacking ordered phase on mechanical properties of Mg97Zn1Y2 extruded alloy. Acta Mater 58:6282–6293

[22] Hagihara K, Kinoshita A, Fukusumi Y, Yamasaki M, Kawamura Y (2013) High-temperature compressive deformation behavior of Mg97Zn1Y2 extruded alloy containing a long-period stacking ordered (LPSO) phase. Mater Sci Eng A 560:71–79

[23] Hagihara K, Yokotani N, Umakoshi Y (2010) Plastic deformation behavior of Mg12YZn with 18R long-period stacking ordered structure. Intermetallics 18:267–276

[24] Yu ZJ, Huang Y, Qiu X, Yang Q, Sun W, Tian Z, Zhang DP, Meng J (2013) Fabrication of magnesium alloy with high strength and heat-resistance by hot extrusion and ageing. Mater Sci Eng A 578:346–353

[25] Yu Z, Huang Y, Qiu X, Wang G, Meng F, Hort N, Meng J (2015) Fabrication of a high strength Mg–11Gd–4.5Y–1Nd–1.5Zn–0.5Zr (wt%) alloy by thermomechanical treatments. Mater Sci Eng A 622:121–130

[26] Pérez-Prado MT, Ruano OA (2003) Texture evolution during grain growth in annealed MG AZ61 alloy. Scr Mater 48:59–64

[27] Pérez-Prado MT, Ruano OA (2002) Texture evolution during annealing of magnesium AZ31 alloy. Scr Mater 46:149–155

[28] Bohlen J, Yi SB, Swiostek J, Letzig D, Brokmeier HG, Kainer KU (2005) Microstructure and texture development

during hydrostatic extrusion of magnesium alloy AZ31. Scr Mater 53:259–264

[29] Stanford N, Atwell D, Beer A, Davies C, Barnett MR (2008) Effect of microalloying with rare-earth elements on the texture of extruded magnesium-based alloys. Scr Mater 59:772–775

[30] Stanford N (2010) Micro-alloying Mg with Y, Ce, Gd and La for texture modification—a comparative study. Mater Sci Eng A 527:2669–2677

[31] Bohlen J, Nürnberg MR, Senn JW, Letzig D, Agnew SR (2007) The texture and anisotropy of magnesium–zinc–rare earth alloy sheets. Acta Mater 55:2101–2112

[32] Humphreys FJ, Hatherly M (1995) Recrystallization and related annealing phenomena. Pergramon, Oxford

[33] Wu WX, Jin L, Zhang ZY, Ding WJ, Dong J (2014) Grain growth and texture evolution during annealing in an indirect-extruded Mg–1Gd alloy. J Alloys Compd 585:111–119

[34] Brokmeier HG (2011) Neutron and photon research for texture and stress characterisation of advanced materials. In: Jiao S, Jiang ZY, Bu JL (eds) Advances in superalloys, Pts 1 and 2. Trans Tech Publications, pp 891–894

[35] Nie JF (2012) Precipitation and hardening in magnesium alloys. Metall Mater Trans A 43:3891–3939

[36] Shao XH, Yang ZQ, Ma XL (2010) Strengthening and toughening mechanisms in Mg–Zn–Y alloy with a long period stacking ordered structure. Acta Mater 58:4760–4771

[37] Hantzsche K, Bohlen J, Wendt J, Kainer KU, Yi SB, Letzig D (2010) Effect of rare earth additions on microstructure and texture development of magnesium alloy sheets. Scr Mater 63:725–730

[38] Stanford N (2013) The effect of rare earth elements on the behaviour of magnesium-based alloys: part 2—recrystallisation and texture development. Mater Sci Eng A 565:469–475

[39] Stanford N, Callaghan MD, de Jong B (2013) The effect of rare earth elements on the behaviour of magnesium-based alloys: part 1—hot deformation behaviour. Mater Sci Eng A 565:459–468

[40] Hadorn JP, Hantzsche K, Yi S, Bohlen J, Letzig D, Wollmershauser JA, Agnew SR (2011) Role of solute in the texture modification during hot deformation of mg–rare earth alloys. Metall Mater Trans A 43:1347–1362

[41] Garcés G, Pérez P, Adeva P (2005) Effect of the extrusion texture on the mechanical behaviour of Mg–SiCp composites. Scr Mater 52:615–619

[42] Wang YN, Huang JC (2003) Texture analysis in hexagonal materials. Mater Chem Phys 81:11–26

[43] Yang Z, Wang ZH, Duan HB, Guo YC, Gao PH, Li JP (2015) Microstructure evolution of Mg–6Gd–2Y alloy during solid solution and aging process. Mater Sci Eng A 631:160–165

[44] Gao Y, Wang Q, Gu J, Zhao Y, Tong Y (2007) Behavior of Mg–15Gd–5Y–0.5Zr alloy during solution heat treatment from 500 to 540 °C. Mater Sci Eng A 459:117–123

[45] Wagner F, Bozzolo N, Van Landuyt O, Grosdidier T (2002) Evolution of recrystallisation texture and microstructure in low alloyed titanium sheets. Acta Mater 50:1245–1259

[46] Alizadeh R, Mahmudi R, Ngan AHW, Langdon TG (2015) Microstructural stability and grain growth kinetics in an extruded fine-grained Mg–Gd–Y–Zr alloy. J Mater Sci 50:4940–4951. doi:10.1007/s10853-015-9041-x

[47] Yi S, Brokmeier H-G, Letzig D (2010) Microstructural evolution during the annealing of an extruded AZ31 magnesium alloy. J Alloys Compd 506:364–371

[48] Xu SW, Oh-ishi K, Kamado S, Uchida F, Homma T, Hono K (2011) High-strength extruded Mg–Al–Ca–Mn alloy. Scr Mater 65:269–272

[49] Yu Z, Huang Y, Gan W, Mendis CL, Zhong Z, Brokmeier HG, Hort N, Meng J (2016) Microstructure evolution of Mg–11Gd–4.5Y–1Nd–1.5Zn–0.5Zr (wt%) alloy during deformation and its effect on strengthening. Mater Sci Eng A 657:259–268

[50] Barnett MR, Keshavarz Z, Beer AG, Atwell D (2004) Influence of grain size on the compressive deformation of wrought Mg–3Al–1Zn. Acta Mater 52:5093–5103

[51] Oh-ishi K, Mendis CL, Homma T, Kamado S, Ohkubo T, Hono K (2009) Bimodally grained microstructure development during hot extrusion of Mg–2.4Zn–0.1Ag–0.1Ca–0.16Zr (at.%) alloys. Acta Mater 57:5593–5604